The Astrophysical Journal, 944:7 (13pp), 2023 February 10 https://doi.org/10.3847/1538-4357/acac31

Constraining the Equation of State of Hybrid Stars Using Recent Information from Multidisciplinary Physics

Swarnim Shirke, Suprovo Ghosh, and Debarati Chatterjee
Inter-University Centre for Astronomy and Astrophysics, Post Bag 4, Ganeshkhind, Pune 411 007, India; debarati@iucaa.in
Received 2022 October 21; revised 2022 December 9; accepted 2022 December 12; published 2023 February 8

Abstract

At the ultrahigh densities existing in the core of neutron stars (NSs), it is expected that a phase transition from baryonic to deconfined quark matter may occur. Such a phase transition would affect the underlying equation of state (EoS) as well as the observable astrophysical properties of NSs. Comparison of EoS model predictions with astronomical data from multimessenger signals then provides us an opportunity to probe the behavior of dense matter. In this work, we restrict the allowed parameter space of EoS models in NSs for both nucleonic (relativistic mean field model) and quark matter (MIT bag model) sectors by imposing state-of-the-art constraints from nuclear calculations, multimessenger astrophysical data, and perturbative quantum chromodynamics (pQCD). We systematically investigate the effect of each constraint on the parameter space of uncertainties using a cutoff filter scheme, as well as the correlations among the parameters and with NS astrophysical observables. Using the constraints, we obtain limits for maximum NS mass, maximum central density, as well as for NS radii and tidal deformability. Although pQCD constraints are only effective at very high densities, they significantly reduce the parameter space of the quark model. We also conclude that astrophysical data supports high values of the bag parameter B and disfavors the existence of a pure quark matter core in hybrid stars.

Unified Astronomy Thesaurus concepts: Neutron stars (1108); Neutron star cores (1107); Gravitational waves (678); High energy astrophysics (739); Particle astrophysics (96)

1. Introduction

One of the most intriguing questions in physics is the fundamental constitution of matter. High-energy experiments are performed in nuclear laboratories, as well as heavy-ion collision experiments in accelerators to probe the nature of matter under extreme conditions of temperature and density, which explore different regions of the phase diagram of quantum chromodynamics (QCDs), the theory of strong interactions (Baym et al. 2018). Despite recent advances (Fodor & Katz 2004; Aoki et al. 2006; Bazavov et al. 2017, 2019), lattice QCD calculations are not applicable at finite chemical potentials due to the sign problem (de Forcrand 2010). Theoretical calculations from chiral effective field theory (CEFT; Drischler et al. 2016, 2019; Keller et al. 2021) for low-density nuclear matter and perturbative QCD (pQCD; Kurkela et al. 2010; Gorda et al. 2018, 2021a, 2021b) for high-density quark matter provide some reliable limits.

An alternative means to approach this problem is through astrophysical systems such as compact stars. Neutron stars (NSs) span a wide range of densities, from nuclei at the surface to several times normal nuclear matter density in the core. NSs provide a natural environment for the appearance of strangeness-containing matter, such as hyperons or deconfined quark matter in its interior, due to the ultrahigh densities prevailing there (Glendenning 1997; Lattimer & Prakash 2004). Therefore, studying NSs provides the possibility of probing hadron–quark phase transition in an astrophysical scenario.

It is conjectured that if a phase transition from hadronic to quark matter (crossover or first order) occurs in the NS interior, it could significantly affect several observable NS properties, such as its mass, radius, moment of inertia, or even gravitational-wave (GW) emission (Alford et al. 2007, 2019; Bauswein et al. 2019). NSs have been observed for many decades at multiple frequencies across the electromagnetic spectrum, from which one can deduce important global properties such as their mass or radius, which can be related to their equation of state (EoS). Precise measurements of the NS maximum mass (Demorest et al. 2010; Antoniadis et al. 2013; Linares et al. 2018; Cromartie et al. 2020; Linares 2020; Fonseca et al. 2021) impose stringent constraints on NS core composition. Although radius measurements from quiescent low-mass X-ray binaries and thermonuclear bursts of accreting NSs suffer from larger uncertainties (Guillot et al. 2013; Özel & Freire 2016; Özel et al. 2016), the NICER mission, recently launched by NASA, is providing radius estimates with much higher accuracy (Miller et al. 2019, 2021; Riley et al. 2019, 2021). Further, a breakthrough has emerged with the recent direct detection of GWs by the LIGO-Virgo Collaboration (Abbott et al. 2017a, 2017b). In particular, the detection of GWs from the binary NS merger GW170817 and the inferred tidal deformability of the component NSs in the inspiral phase has led to important implications for the EoS of dense matter (Abbott et al. 2017a, 2017b, 2019). NS multimessenger observations can therefore provide a wealth of information about NSs' internal composition (Bauswein et al. 2017; Margalit & Metzger 2017; Annala et al. 2018; Fattoyev et al. 2018; Most et al. 2018; Paschalidis et al. 2018; Radice et al. 2018; Rezzolla et al. 2018).

It was shown that imposing complementary limiting constraints at high densities from pQCD in addition to low-density nuclear matter from CEFT reduces the uncertainty of NS matter significantly (Kurkela et al. 2014; Komoltsev & Kurkela 2022). The highest observed NS mass $\sim 2\ M_{\odot}$ (Demorest et al. 2010; Antoniadis et al. 2013; Cromartie et al. 2020; Fonseca et al. 2021) further imposes important consequences on the speed of sound for

a given EoS. Combining additional constraints from tidal deformability dramatically reduces the allowed parameter space of EoS (Annala et al. 2018). In such studies, EoS employed to interpolate between the low- and high-density limits were piecewise polytropes or Chebyshev polynomials. Combining astrophysical observations with theoretical ab initio calculations in a model-independent way, the behavior of the speed of sound was used to establish evidence of the presence of quark matter cores in NSs (Annala et al. 2020). Other multimessenger NS data, e.g., measurements of pulsar radii from X-ray (Bogdanov et al. 2016; Nättilä et al. 2017) or NICER observations (Miller et al. 2019, 2021; Riley et al. 2019, 2021) has also been employed to impose strong constraints on the EoS and to test the presence of quark matter in NSs (Annala et al. 2022).

The effect of phase transition in supranuclear matter on the GW signal is being studied with great interest (Chatziioannou & Han 2020; Pang et al. 2020). Over the past couple of years, several works have used a Bayesian statistical approach to incorporate prior knowledge of multimessenger data to perform a joint analysis of GW signals and their electromagnetic counterparts, combined with X-ray and radio pulsar observations and nuclear-theory calculations (Coughlin et al. 2019; Radice & Dai 2019; Dietrich et al. 2020; Raaijmakers et al. 2020). Such studies have also been extended to investigate quark stars (Zhou et al. 2018; Li et al. 2020) or hybrid stars (Pang et al. 2021; Xie & Li 2021). This is usually done by employing piecewise polytropes or constant speed-of-sound parameterization (Alford et al. 2013). The drawback of such a scheme is that the constrained parameters (e.g., the speed of sound or polytropic index) cannot be directly linked to the properties of the microscopic quark matter EoS, or the correlations of the underlying hadronic or quark parameters with global NS observables cannot be investigated.

A few recent studies have considered hybrid stars with a phase transition from hadronic models based on nuclear interactions (such as the relativistic mean field, RMF) to quark matter models (such as the MIT bag model or extended linear sigma model; Nandi & Char 2018; Nandi & Pal 2021; Parisi et al. 2021; Kovács et al. 2022). These works imposed constraints from NS maximum mass and tidal deformability in the light of GW170817 to constrain the model parameters. However, such works only considered selected EoS models (several of which are now incompatible with recent astrophysical data), which do not necessarily span the allowed parameter space of the hadronic/quark EoS.

In two recent publications (Ghosh et al. 2022a, 2022b), the authors of this paper (S.G. and D.C.) explored the parameter space of hadronic matter within the framework of the RMF model allowed by present uncertainties compatible with state-of-the-art nuclear/hypernuclear experimental data. They applied a Bayesian-like scheme with a hard cutoff to constrain the parameter space using multiphysics constraints at different density regimes: CEFT, nuclear and heavy-ion collision data, as well as multimessenger astrophysical observations of NSs. Using the posterior distributions, they investigated possible correlations between nuclear, hypernuclear, and astrophysical observables. This work extends this scheme to the quark degrees of freedom. By varying the parameters of the hadronic (RMF) and quark (MIT bag) models within their present uncertainties, constraints are imposed using CEFT at low densities, multimessenger astrophysical data at high densities, and pQCD at very high densities. We then investigate possible correlations among the model parameters as well as with NS global observables.

The paper is structured as follows. In Section 2, we outline the formalism used to carry out this study. In particular, we explain the microscopics of the generated EoS in Section 2.1, the global properties of NSs in Section 2.2, and the details of the Bayesian scheme followed and constraints applied in Section 2.3. We present the results of the work in Section 3. The final section, Section 4, discusses the implications of these results and important findings.

2. Formalism

2.1. Microscopic Description

There are different approaches to describing dense nuclear matter in NSs (Oertel et al. 2017). While the ab initio techniques employ calculations of nucleon–nucleon two-body interactions, the density functional models apply phenomenological techniques by adjusting model parameters to reproduce experimental nuclear observables. Similarly, there exist different descriptions for the pure quark matter phase, effective theories such as the Nambu–Jona-Lasinio model (Nambu & Jona-Lasinio 1961a, 1961b), or phenomenological models such as the MIT bag model (Chodos et al. 1974b; Farhi & Jaffe 1984). In this work, a phenomenological RMF model is used to describe the pure nucleonic phase, while the pure quark phase is described using the phenomenological MIT bag model (Chodos et al. 1974a, 1974b; Farhi & Jaffe 1984). The mixed phase is constructed by applying Gibbs phase rules (Glendenning 1997). NS matter in all phases is subject to chemical beta equilibrium and charge neutrality constraints. These phases are elaborated on in the sections below.

2.1.1. Pure Nucleonic Phase

To solve for the EoS of finite nucleonic matter, we adopt the RMF model with nucleons (N), i.e., protons (p) and neutrons (n), and their interactions given by the exchange of three meson fields: scalar sigma (σ), vector omega (ω), and isovector rho (ρ) (Glendenning & Moszkowski 1991; Fattoyev & Piekarewicz 2010; Chen & Piekarewicz 2014; Hornick et al. 2018). Leptons (l) present in the matter (here electrons and muons) are free and noninteracting (Weber 1999). The interaction Lagrangian is

$$\begin{aligned}\mathcal{L}_{\rm int} = &\sum_N \bar{\psi}_N \left[g_\sigma \sigma - g_\omega \gamma^\mu \omega_\mu - \frac{g_\rho}{2} \gamma^\mu \boldsymbol{\tau} \cdot \boldsymbol{\rho}_\mu \right] \psi_N \\ &- \frac{1}{3} b m_N (g_\sigma \sigma)^3 - \frac{1}{4} c (g_\sigma \sigma)^4 \\ &+ \Lambda_\omega (g_\rho^2 \boldsymbol{\rho}^\mu \cdot \boldsymbol{\rho}_\mu)(g_\omega^2 \omega^\nu \omega_\nu) + \frac{\zeta}{4!} (g_\omega^2 \omega^\mu \omega_\mu)^2, \end{aligned} \quad (1)$$

where ψ is the Dirac spinor for fermions, m_N is the vacuum nucleon mass, $\{\gamma^i\}$ are the gamma matrices, $\boldsymbol{\tau}$ are Pauli matrices. g_σ, g_ω, and g_ρ are meson–nucleon coupling constants. The scalar and vector self-interactions couplings are b, c, and ζ, respectively, while Λ_ω is the vector–isovector interaction. In the mean-field approximation, the mesonic fields are replaced by their expectation values, $\bar{\sigma} = \langle \sigma \rangle$, $\bar{\omega} = \langle \omega^0 \rangle$, $\bar{\rho} = \langle \rho_3^0 \rangle$, in the ground state. The field equations are solved to obtain the

energy density (ϵ) (Hornick et al. 2018):

$$\epsilon = \sum_N \frac{1}{8\pi^2}\left[k_{F_N}E_{F_N}^3 + k_{F_N}^3 E_{F_N} - m^{*4}\ln\left(\frac{k_{F_N}+E_{F_N}}{m^*}\right)\right] + \frac{1}{2}m_\sigma^2\bar{\sigma}^2 + \frac{1}{2}m_\omega^2\bar{\omega}^2 + \frac{1}{2}m_\rho^2\bar{\rho}^2 + \frac{1}{3}bm_N(g_\sigma\bar{\sigma})^3 + \frac{1}{4}c(g_\sigma\bar{\sigma})^4 + 3\Lambda_\omega(g_\rho g_\omega\bar{\rho}\bar{\omega})^2 + \frac{\zeta}{8}(g_\omega\bar{\omega})^4, \quad (2)$$

where

$$E_{F_N} = \sqrt{k_{F_N}^2 + m^{*2}},$$
$$m^* = m_N - g_\sigma\sigma,$$
$$\mu_N = E_{F_N} + g_\omega\bar{\omega} + \frac{g_\rho}{2}\tau_{3N}\bar{\rho}. \quad (3)$$

Here, k_{F_N} is the Fermi momentum, E_{F_N} is the Fermi energy, and μ_N is the chemical potential of nucleon N. m^* is the effective nucleon mass. The pressure, P, is obtained using the Gibbs–Duhem relation:

$$P = \sum_N \mu_N n_N - \epsilon. \quad (4)$$

We also add to this the contribution from leptons. In this work, the vector self-interaction (ζ) term has been set to zero as it is known to soften the EoS (Müller & Serot 1996; Tolos et al. 2017; Keshari Pradhan et al. 2023).

In order to generate an EoS, we need to know the coupling constants (g_σ, g_ω, g_ρ, b, c, Λ_ω) in the Lagrangian. The isoscalar couplings (g_σ, g_ω, b, c) are fitted using the nuclear saturation parameters ($n_{\rm sat}$, $E_{\rm sat}$, $K_{\rm sat}$, and m^*) obtained from experiments. Similarly, the isovector couplings (g_ρ, Λ_ω) are fitted to the symmetry properties ($E_{\rm sym}$, $L_{\rm sym}$) of nuclear matter at saturation (Chen & Piekarewicz 2014; Hornick et al. 2018). The empirical parameters in the pure nucleonic phase are therefore $\{n_{\rm sat}, E_{\rm sat}, K_{\rm sat}, E_{\rm sym}, L_{\rm sym}, m^*\}$.

2.1.2. Pure Quark Phase

For the pure quark phase, we use the MIT bag model with first-order strong interaction corrections (Farhi & Jaffe 1984). The grand potential density (($\Omega = -P$); Farhi & Jaffe 1984; Glendenning 1997) is given by

$$\Omega = \sum_{f=u,d,s}\Omega_f + \sum_{l=e,\mu}\Omega_{l,\rm free} + B, \quad (5)$$

where $\Omega_{i,\rm free}$ is the grand potential of free Fermi gas, and

$$\Omega_i = \Omega_{i,\rm free} + \frac{1}{4\pi^2}\frac{2\alpha}{\pi}\left[3\left(\mu_i k_{F_i} - m_i^2\ln\frac{\mu_i+k_{F_i}}{\mu_i}\right)^2 - 2k_{F_i}^4 - 3m_i^4\ln^2\frac{m_i}{\mu_i} + 6\ln\frac{\tilde{\Lambda}}{\mu_i}\left(m_i^2\mu_i k_{F_i} - m_i^4\ln\frac{\mu_i+k_{F_i}}{m_i}\right)\right]. \quad (6)$$

The energy density is calculated using Equation (4). α_s is the strong interaction coupling, and $\tilde{\Lambda}$ is the QCD renormalization scale, set to 300 MeV. We define $a_4 = 1 - 2\alpha_s/\pi$. The empirical parameters for the pure quark phase are the bag parameters $\{B^{1/4}, a_4\}$.

2.1.3. Mixed Phase: Gibbs Construction

In the quark deconfinement transition, two quantities are conserved: the baryon number and the total electric charge. Thus, we can characterize the phase transition by the Gibbs construction (Glendenning 1997), where the hadronic matter and quark matter can coexist and is given by the condition

$$P_H(\mu_b, \mu_q) = P_Q(\mu_b, \mu_q). \quad (7)$$

Here, P_H and P_Q are the pressures of the hadron and quark phases, respectively, μ_b is the baryon chemical potential, and μ_q is the charge chemical potential. If we consider global charge conservation, we have the equations of constraint, given by

$$\chi q^Q + (1-\chi)q^H = 0,$$
$$\chi n^Q + (1-\chi)n^H = n_B, \quad (8)$$

where Q stands for all quarks in the deconfined phase, H stands for hadrons and leptons in the confined phase, with n and q denoting the number density and electric charge, respectively. n_B is the total baryon number density. The volume fraction (χ) is defined as $\chi = V_Q/(V_Q + V_H)$ for quarks, and the hadron volume fraction is given by $1-\chi$. The total energy density in the mixed phase is given by

$$\epsilon = \chi\epsilon^Q + (1-\chi)\epsilon^H.$$

2.2. Macroscopic Structure

To calculate the mass (M) and radius (R) of nonrotating hybrid stars, we solve the Tolman–Oppenheimer–Volkoff (TOV) equations (Glendenning 1997; Schaffner-Bielich 2020):

$$\frac{dP(r)}{dr} = -\frac{[P(r)+\epsilon(r)][m(r)+4\pi r^3P(r)]}{r(r-2m(r))},$$
$$\frac{dm(r)}{dr} = 4\pi r^2\epsilon(r), \quad (9)$$

along with the equation state, applying the boundary conditions $m(r=0)=0$ and $P(r=R)=0$. The dimensionless tidal deformability (Λ) is defined as

$$\Lambda = \frac{2}{3}\frac{k_2}{C^5}, \quad (10)$$

where $C = GM/Rc^2$ is the dimensionless compactness. To calculate this we solve for the $l=2$ Love number k_2 as done in Flanagan & Hinderer (2008), Hinderer (2008), Damour & Nagar (2009), and Yagi & Yunes (2013).

2.3. Cutoff Filter Scheme

In this study, we apply a "cutoff filter" scheme, wherein we impose strict limits demanding compatibility with nuclear and astrophysical observational data to obtain the posteriors. As in Bayesian analysis, the priors are obtained by varying the empirical nuclear and quark model parameters described in Section 2.3.1, and the likelihood functions are appropriately chosen physical conditions as filter functions, as explained in Section 2.3.2. We then use the posterior sets to calculate

Table 1
The Range of Variation of Empirical Nuclear and Bag Model Parameters within their Present Uncertainties

n_{sat} (fm^{-3})	E_{sat} (MeV)	K_{sat} (MeV)	E_{sym} (MeV)	L_{sym} (MeV)	m^*/m	a_4	$B^{1/4}$ (MeV)
0.14–0.17	-16.0 ± 0.2	200–300	28–34	40–70	0.55–0.75	0.4–1.0	100–300

Note. Meson masses are set to $m_\sigma = 550$ MeV, $m_\omega = 783$ MeV, and $m_\rho = 770$ MeV; the quark masses to $m_u = 5$ MeV, $m_d = 5$ MeV, and $m_s = 100$ MeV; and the nucleon mass is set to $m_N = 939$ MeV.

correlations (Section 2.3.3). In our previous work (Ghosh et al. 2022a), it was explicitly demonstrated that including the statistical reweighting using χ-squared statistics might change the posterior probability distribution slightly, but it does not significantly alter the physical correlation between nuclear empirical parameters and astrophysical observables. Many other works have followed the same scheme (Kurkela et al. 2014; Annala et al. 2018, 2020; Most et al. 2018; Ghosh et al. 2022b). A similar scheme was employed to study the correlations between nuclear parameters in various works (Chatterjee et al. 2017; Margueron et al. 2018; Ghosh et al. 2022a, 2022b). We adopt this cutoff filter scheme for this investigation.

2.3.1. Priors

As explained in Sections 2.1.1 and 2.1.2, the combined set of empirical parameters is $\{n_{sat}, E_{sat}, K_{sat}, E_{sym}, L_{sym}, m^*, B^{1/4}, a_4\}$. We vary these model parameters uniformly (flat prior) within a prior range given in Table 1, as was done in our previous work (Ghosh et al. 2022a).

We generate EoS with model parameters randomly varied in the range shown in Table 1. The range of variation is as used in our previous work (Ghosh et al. 2022a) given by state-of-the-art nuclear experimental data (Oertel et al. 2017; Hornick et al. 2018). The range for parameter a_4 is chosen so that at $a_4 = 1$, $\alpha_s = 0$ and for $a_4 = 1$, $\alpha_s \approx 1$, beyond which perturbation theory does not apply. A wide range of values is considered for $B^{1/4}$ (100–300 MeV). The lower limit is set to $B^{1/4} = 100$ MeV, as for lower values the mixed phase begins within the crust (Nandi & Char 2018). For large values of the bag constant, the hybrid EoS asymptotically resembles the pure nucleonic EoS, as the mixed phase is not reached for the densities attained in the NS interior. We set an upper limit of $B^{1/4} = 300$ MeV, as done in Weissenborn et al. (2011).

2.3.2. Constraints

First, for an EoS generated for a set of model parameters, we check if it is physical by verifying that it satisfies the physical conditions such as positive-definiteness of pressure, energy, speed of sound, and causality ($c_s^2 < 1$). We then apply various cutoff filters to constrain the model parameter space. The following multiphysics constraints are used in this work:

1. *CEFT at low densities.*
   The EoS at low densities (0.07–0.20 fm^{-3}) is constrained using recent calculations from CEFT (Drischler et al. 2019). CEFT takes into account the many-body interactions and solves for the nuclear forces in the low-momentum limit. These microscopic calculations are only valid for pure neutron matter (PNM). We construct the PNM EoS using the nuclear saturation parameters from Table 1 and compare it with the CEFT calculations. If the EoS falls in the CEFT uncertainty band, we retain this set of parameters, which is then used to construct hybrid EoS for varying bag parameters. These hybrid EoS are further checked for consistency with other constraints explained below.
2. *Astrophysical observations at high densities.*
   In this study, we use the following state-of-the-art multimessenger (electromagnetic and GW) astrophysical observations:
   (a) A recent observation of the high-mass pulsar PSR J0740+6620 estimates its mass to be $2.08^{+0.07}_{-0.07} M_\odot$ (Fonseca et al. 2021), the errors indicating a 1σ interval. Very recently, a heavy galactic NS was found with a mass 2.35 ± 0.17 $M_\odot$ having a relatively larger error (Romani et al. 2022). In this work, we use the conservative lower limit of 2.01 $M_\odot$ for the maximum NS mass.
   (b) The GW signal from the binary NS merger event GW170817 (Abbott et al. 2017a, 2017b) has been analyzed to obtain various properties of the constituent NSs (Abbott et al. 2019) such as tidal deformability. The tidal deformability of a 1.4 $M_\odot$ NS ($\Lambda_{1.4M_\odot}$) is estimated to be less than 580 (Abbott et al. 2018) with 90% confidence. For any given EoS, we calculate Λ for the mass of 1.4 $M_\odot$, and this value should fall below 580 in order to say that it satisfies this constraint.
3. *pQCD at very high densities.*
   The EoS of cold, dense matter can be calculated at very high densities using perturbative techniques. To impose this constraint on our EoS, we use the parameterization of the pressure as a function of chemical potential using a fitting function for cold quark matter (Fraga et al. 2014), which depends on the renormalization scale $\tilde{\Lambda}$:

$$P(\mu_B) = P_{\rm free}(\mu_B)\left(c_1 - \frac{a(X)}{(\mu_B/\mathrm{GeV}) - b(X)}\right), \tag{11}$$

$$a(X) = d_1 X^{-\nu_1}, \quad b(X) = d_2 X^{-\nu_2}, \tag{12}$$

where $P_{\rm free}$ is the pressure of the three noninteracting massless quarks:

$$P_{\rm free}(\mu_B) = \frac{3}{4\pi^2}\left(\frac{\mu_B}{3}\right)^4. \tag{13}$$

X is a dimensionless parameter that depends on the renormalization scale as $X \equiv 3\tilde{\Lambda}/\mu_B$, which belongs to the range $X \in [1, 4]$ for a good fit. The best-fit parameters are given by Fraga et al. (2014):

$$c_1 = 0.9008,\ d_1 = 0.5034,\ d_2 = 1.452,$$
$$\nu_1 = 0.3553;\ \nu_2 = 0.9101. \tag{14}$$

For a set of empirical parameters, we generate the EoS up

to high densities. For baryon chemical potentials $\mu_B = 2.6$ GeV (corresponding to baryonic number densities $n_B \geqslant 40 n_{\rm sat}$), we verify the pressure of the hybrid EoS falls within the pQCD range, i.e., matches the pQCD pressure for some value of $X \in [1, 4]$. We verify that we obtain $n_B \gtrsim 40 n_{\rm sat}$ at $\mu_B = 2.6$ GeV and that the conformal limit for the speed of sound is not violated at high densities.

There are more recent calculations for the QCD pressure, e.g., up to next-to-next-to-next-to-leading order (N^3LO) for cold quark matter (Gorda et al. 2021a, 2021b). The results do not significantly differ from the calculation up to the second order in the strong coupling constant, $\mathcal{O}(\alpha_s^2)$, i.e., N^2LO (Kurkela et al. 2010; Fraga et al. 2014), so these improvements are not expected to have a strong impact on constraining the EoS at NS densities.

2.3.3. Correlations

After applying the filter functions mentioned in the previous section, only the EoS satisfying the constraints survive, which we call the posterior set. Using this posterior, we can study the correlations between the physical parameters of the model among themselves and with the NS observables like mass, radius, and tidal deformability. We evaluate the Pearson's correlation coefficient between a pair of quantities, X and Y, as

$$r_{XY} = \frac{\mathrm{Cov}(X, Y)}{\sqrt{\mathrm{Cov}(X, X)}\sqrt{\mathrm{Cov}(Y, Y)}}.$$

$\mathrm{Cov}(X, Y)$ is the covariance between the quantities X and Y, defined as

$$\mathrm{Cov}(X, Y) = \frac{1}{N}\sum_{i=1}^{N}(X_i - \bar{X})(Y_i - \bar{Y}),$$

where $\bar{X}$ is the sample mean, given by $\bar{X} = \frac{1}{N}\sum_i X_i$.

3. Results

For each EoS, we generate the corresponding PNM EoS using only the nuclear parameters. The posterior set of EoSs that satisfies CEFT constraint and other physical conditions such as positivity of pressure, energy, speed of sound, and causality ($c_s^2 < 1$) is referred to as "CEFT." Out of the 100,000 parameter sets, about 23% satisfy these constraints. The posterior set is then passed through astrophysical constraint filters, outlined in Section 2.3.2 and referred to as "Astro." This scheme allows 31% of the EoS from the CEFT posterior set. If we only add the pQCD constraint instead of astrophysical ones, we are left with 52%. Finally, both the astrophysical and pQCD constraints are applied, permitting approximately 16% EoS through both filters.

3.1. Posteriors

For the posterior sets obtained after passing through the different constraint filters, we analyze the range of densities and baryon chemical potentials in the NS core. For the maximum-mass configuration for each EoS, the minimum and maximum values of the central density ($n_{\rm cen}$) and the corresponding baryon chemical potential ($\mu_{\rm cen}$) are provided in Table 2. The values are compatible with those in Kurkela et al. (2014), where a maximum central density of 8.0 $n_{\rm sat}$ was obtained, although we find an upper bound on $\mu_{\rm cen}$ that is higher by 0.2 GeV. We also note down the range of maximum mass ($M_{\rm max}$), radius ($R_{1.4M_\odot}$) and tidal deformability ($\Lambda_{1.4M_\odot}$) from the posterior set in Table 2.

In the following section, we display the posteriors obtained after passing the prior sample through the different constraint filters. In Figure 1, the EoS is represented by the pressure plotted as a function of baryon chemical potential. A broad blue band is obtained for EoS with the imposition of CEFT alone. As CEFT constrains the EoS only at low densities, the band broadens at higher chemical potentials. The addition of astrophysical constraints narrows the band further (orange), particularly at intermediate densities up to $\mu_B = 1.5$ GeV, beyond which the band broadens again. At higher chemical potentials, the solutions obtained are unstable. Although pQCD constricts the band at higher densities (green) beyond $\sim\mu_B = 2.0$ GeV, such densities are not reached in the NS interior (refer to Table 2). Below $\sim\mu_B = 1.5$ GeV, the pQCD cloud coincides with the orange cloud, and it is not very constraining below $\mu_B = 2.0$ GeV. This can be verified from

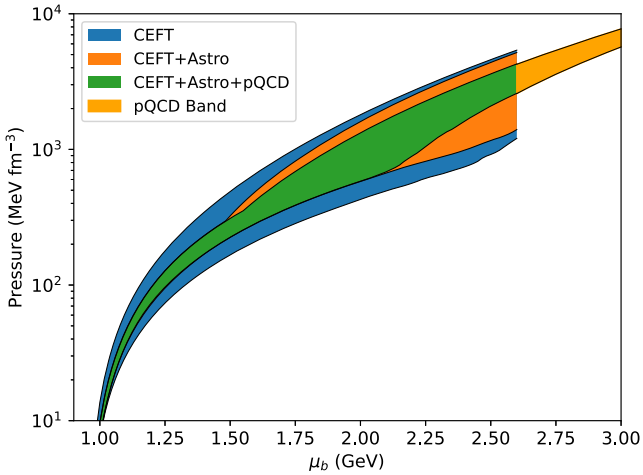

Figure 1. EoS (pressure vs. baryon chemical potential) contours obtained on imposing filters from Section 2.3.2. The blue contour is obtained after enforcing only CEFT and minimal physics constraints, the orange contour on further imposing astrophysical constraints, while the green contour when we additionally impose the pQCD constraint.

Table 2
The Range of Values Observed after Application of Different Filters

Posterior	$n_{\rm cen}$ (fm^{-3})	$\mu_{\rm cen}$ (GeV)	$M_{\rm max}$ ($M_\odot$)	$R_{1.4M_\odot}$ (km)	$\Lambda_{1.4M_\odot}$
CEFT	0.54–1.77	1.13–1.98	1.04–2.99	8.8–14.2	33–1263
CEFT+Astro	0.76–1.23	1.38–1.97	2.01-2.53	11.3–13.1	247–580
CEFT+Astro+pQCD	0.76–1.23	1.39–1.96	2.01–2.52	11.4–13.1	247–580

Note. The range for central density ($n_{\rm cen}$) and chemical potential ($\mu_{\rm cen}$) reached inside a maximally massive NS, maximum TOV mass ($M_{\rm max}$), radius ($R_{1.4M_\odot}$), and tidal deformability ($\Lambda_{1.4M_\odot}$) of a 1.4 $M_\odot$ for each posterior set have been mentioned. The first row corresponds to the CEFT posterior set containing EoS that satisfy CEFT constraints and physical requirements. The second row corresponds to the CEFT+Astro set, where we add the astrophysical constraints ($M \geqslant 2.01\,M_\odot$ and $\Lambda_{1.4M_\odot} \leqslant 580$). The last row corresponds to the CEFT+Astro+pQCD set of EoS that additionally satisfies the constraint from pQCD at high densities.

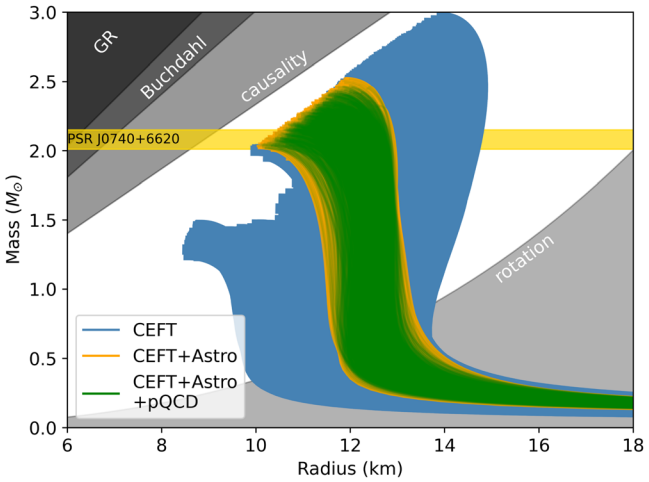

Figure 2. Mass–radius contours corresponding to the EoS contours shown in Figure 1.

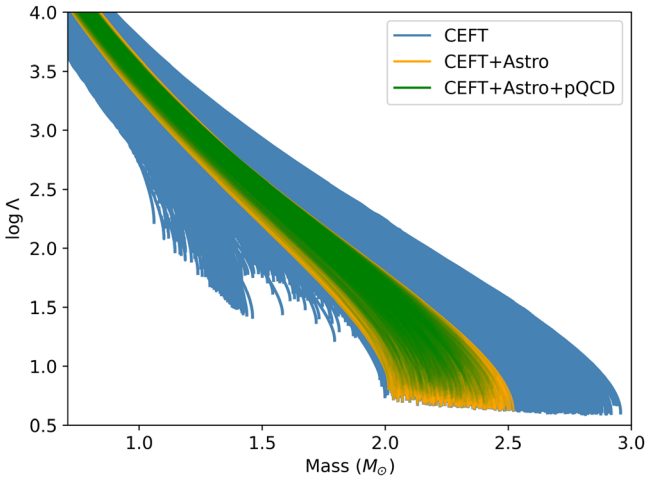

Figure 3. Dimensionless tidal deformability–mass contours corresponding to the EoS contours shown in Figure 1.

Figures 2 and 3, where we plot the mass versus radius and tidal deformability versus mass contours, respectively, for the EoS contours corresponding to Figure 1. We can observe that the addition of pQCD constraints only weakly affects the NS observables, i.e., the orange and green bands nearly coincide. It is well known that pQCD is most instrumental when constraining the higher-density regime of the EoS. However, the pQCD constraint does improve our understanding of the model parameters, as we discuss later.

3.2. Correlation Study

Using the posterior sets discussed in the previous section, we investigate possible correlations among the empirical parameters of both the nuclear ($n_{\rm sat}$, $E_{\rm sat}$, $K_{\rm sat}$, $E_{\rm sym}$, $L_{\rm sym}$, m^*/m), and the quark model ($B^{1/4}$, a_4), as well as with the NS observables ($M_{\rm max}$, R, $R_{1.4\,M_\odot}$, $R_{2\,M_\odot}$, $\Lambda_{1.4\,M_\odot}$, $\Lambda_{2\,M_\odot}$), where R is the radius corresponding to $M_{\rm max}$. From a plot of the correlation coefficient matrix in Figure 4 after applying CEFT constraints, we draw the following conclusions:

1. All NS observables are strongly correlated with each other (>0.9), although the correlations of $M_{\rm max}$ are relatively smaller (0.6–0.8).
2. $n_{\rm sat}$ is moderately correlated with the NS observables of 1.4 $M_\odot$ and 2 $M_\odot$ (∼0.4). The correlation with $R_{1.4\,M_\odot}$ is noticeable (0.46), that with R is weak (0.26), and that with $M_{\rm max}$ is negligible. There is a weak correlation between $L_{\rm sym}$ and $R_{1.4\,M_\odot}$ (0.32). m^*/m is strongly correlated with NS observables (0.7–0.9) but is only moderately correlated with $M_{\rm max}$ (∼0.4).
3. $E_{\rm sym}$ and $L_{\rm sym}$ show moderate correlation (0.63).
4. $M_{\rm max}$ is moderately correlated with $B^{1/4}$ (0.63) and weakly with a_4 (0.28). We do not find a correlation of $B^{1/4}$ and a_4 with any other NS observable or empirical nuclear parameter.

We then add the astrophysical constraint filters as explained in Section 2.3.2. We plot the correlation matrix from this posterior in Figure 5 and observe the following changes:

1. The correlation between $M_{\rm max}$ and R reduces from 0.61 to 0.39. Those between the rest of the NS observables stay unaltered.

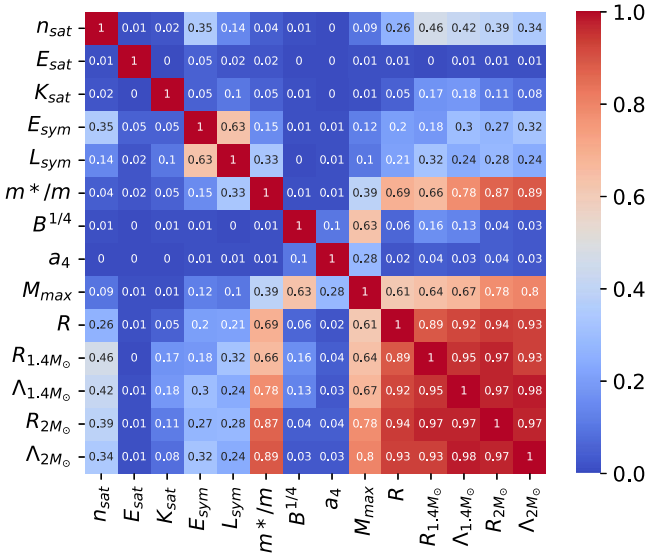

Figure 4. Correlation coefficients between the nuclear and quark model parameters along with the NS observables. These are after applying the CEFT and minimal physics filters.

2. The correlations of $n_{\rm sat}$ with NS observables become weak ($\lesssim$0.3) except for that with $R_{1.4\,M_\odot}$ (0.48). The correlation between $L_{\rm sym}$ and $R_{1.4\,M_\odot}$ remains unaffected (0.35). The correlation between m^*/m and $M_{\rm max}$ becomes strong as it increases from 0.39 to 0.7, making m^*/m the most important parameter in determining NS observables. The correlation between m^*/m and $R_{1.4\,M_\odot}$ reduces from 0.66 to 0.35.
3. A moderate correlation between $n_{\rm sat}$ and m^*/m appears (0.42). $E_{\rm sym}$ and $L_{\rm sym}$ now show a strong correlation (0.71).
4. The correlation of $M_{\rm max}$ with $B^{1/4}$ becomes weak (0.27) and that with a_4 becomes negligible (0.13). Weak correlations appear for R with $B^{1/4}$ (0.35) and a_4 (0.26). $B^{1/4}$ and a_4 become weakly correlated (0.36).

Similar conclusions about the correlations between nuclear and astrophysical observables were drawn in Ghosh et al. (2022a). For the pure nucleonic EoS, $L_{\rm sym}$ and $E_{\rm sym}$ showed strong correlation and a moderate correlation between $L_{\rm sym}$ and

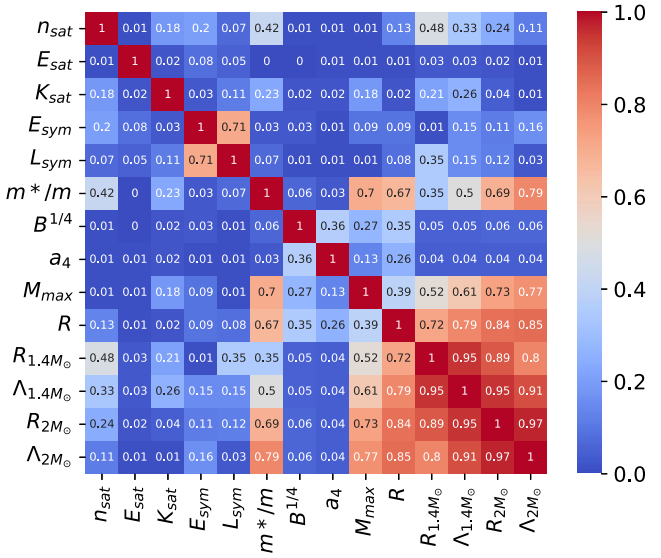

Figure 5. Posterior correlation matrix of the nuclear and quark model parameters along with the NS observables after the application of CEFT and astrophysical constraints filters as explained in Section 2.3.2.

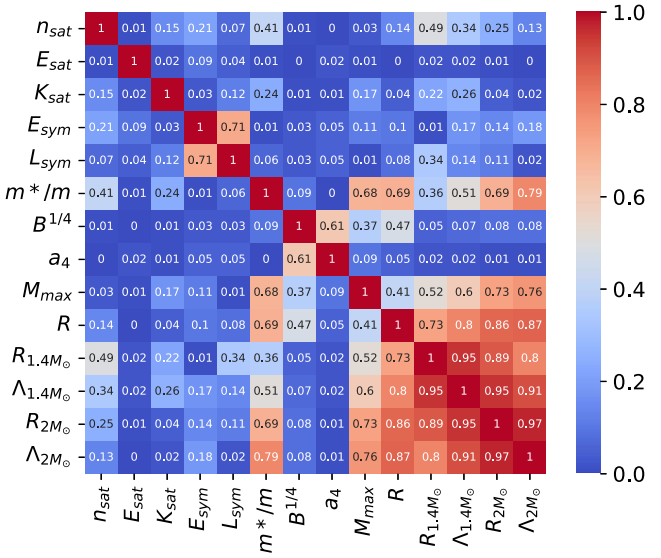

Figure 6. The correlation matrix, same as in Figure 5, after imposing the pQCD filter as explained in Section 2.3.2.

m^*/m was observed (see Figure 5 in Ghosh et al. 2022a), which was due to the CEFT filter. For astrophysical observables, $n_{\rm sat}$ and m^*/m had significant correlations, although the correlation with $n_{\rm sat}$ was much weaker for $2\,M_\odot$ stars. Here also for NSs with a hybrid EoS, we observe similar correlations between the nuclear parameters and astrophysical observables. The correlation between R and Λ of 1.4 and 2 $M_\odot$ stars is expected from Equation (10). Several studies reported a correlation between $L_{\rm sym}$ and $R_{1.4\,M_\odot}$ (Fattoyev et al. 2013; Alam et al. 2016; Lim & Holt 2018; Zhu et al. 2018). Zhang & Li (2019) also looked for a relation between $L_{\rm sym}$, $R_{1.4\,M_\odot}$, and $\Lambda_{1.4\,M_\odot}$ However, our finding is consistent with more recent studies, which find them to be nearly independent (Hornick et al. 2018; Ghosh et al. 2022a, 2022b). A recent study by Biswas (2021) also reported a weak correlation between $L_{\rm sym}$ and $R_{1.4\,M_\odot}$, where laboratory experiments and astrophysical observations, including NICER observations, were used in a Bayesian framework. Our results are also in agreement with Hornick et al. (2018), where it was concluded that m^*/m is more important in determining $R_{1.4\,M_\odot}$ than $L_{\rm sym}$ when CEFT effects are considered. Lower values of m^*/m stiffen the EoS and, thus, raises the maximum mass and radius. This follows from the Hugenholtz–van-Hove theorem explained in Hornick et al. (2018). When quark matter is included in the model, we find that $M_{\rm max}$ is controlled more by $B^{1/4}$ than m^*/m when only CEFT effects are included (see Figure 4). However, inclusion of astrophysical constraints makes m^*/m the most dominant parameter for determining NS observables (see Figure 5).

Finally, in Figure 6 we plot the correlation matrix after additionally imposing the pQCD constraint, and conclude the following:

1. The correlations of nuclear empirical parameters and NS observables remain unaffected.
2. The correlations of $B^{1/4}$ with $M_{\rm max}$ and R increase to 0.37 and 0.47, respectively. Correlation of a_4 with R becomes negligible. We do not find a correlation of a_4 with any parameter, except for a moderate correlation (0.61) with $B^{1/4}$.

For a better understanding, we show the posterior distributions of empirical parameters ($n_{\rm sat}$, $L_{\rm sym}$, m^*/m, $B^{1/4}$, and a_4) and NS observables in a corner plot (Figure 7). We observe from the corner plot that lower values of $L_{\rm sym}$ and m^*/m are disfavored (compared with a flat prior) just after imposing CEFT constraints. This is consistent with the findings of Hornick et al. (2018) and Ghosh et al. (2022a), as low values lead to unphysical EoS. Hornick et al. (2018) also showed that for values of $L_{\rm sym}$ larger than about 60, the EoS falls outside the CEFT band. Values of $L_{\rm sym} \gtrsim 60$ MeV are incompatible with combined constraints from terrestrial experiments, astrophysical observations, and theoretical calculations (Lattimer & Lim 2013) although the PREX II experiment implies a much higher value of $L_{\rm sym} = 106 \pm 37$ MeV (Reed et al. 2021) from the measurement NS thickness of ^{208}Pb (Adhikari et al. 2021). Adding quark degrees of freedom softens the EoS and lowers the mass of the NS. We can expect m^*/m to reduce to compensate for this effect. Within the uncertainty range of the empirical parameters of this study, however, we can have stiff EoS without requiring a low value of m^*/m. The excessive softening of the EoS is countered by a delayed onset of the hadron–quark phase transition achieved mainly from higher values of $B^{1/4}$ and lower values of a_4 (Weissenborn et al. 2011). Thus, the distribution of $B^{1/4}$ shifts to higher values, and that of a_4 shifts slightly to lower values (also see Figure 8) after adding astrophysical constraints. We observe that the distribution is not flat for the CEFT case of $B^{1/4}$. This is because low values of $B^{1/4}$ are unphysical, where the mixed phase begins within the crust. Particularly interesting is the posterior distribution of the a_4 parameter, which becomes peaked only after imposing the pQCD constraint. The normalized, smoothened posterior distributions of a_4 after the application of various filters are highlighted in Figure 8. The EoS falls outside the pQCD band for extreme values of a_4, and the distribution peaks roughly in the central area (0.55–0.85).

3.3. Implications for the Quark EoS

We further investigate the constraints on the $B^{1/4}$–a_4 plane (Figure 9) upon imposition of pQCD constraints. No physical

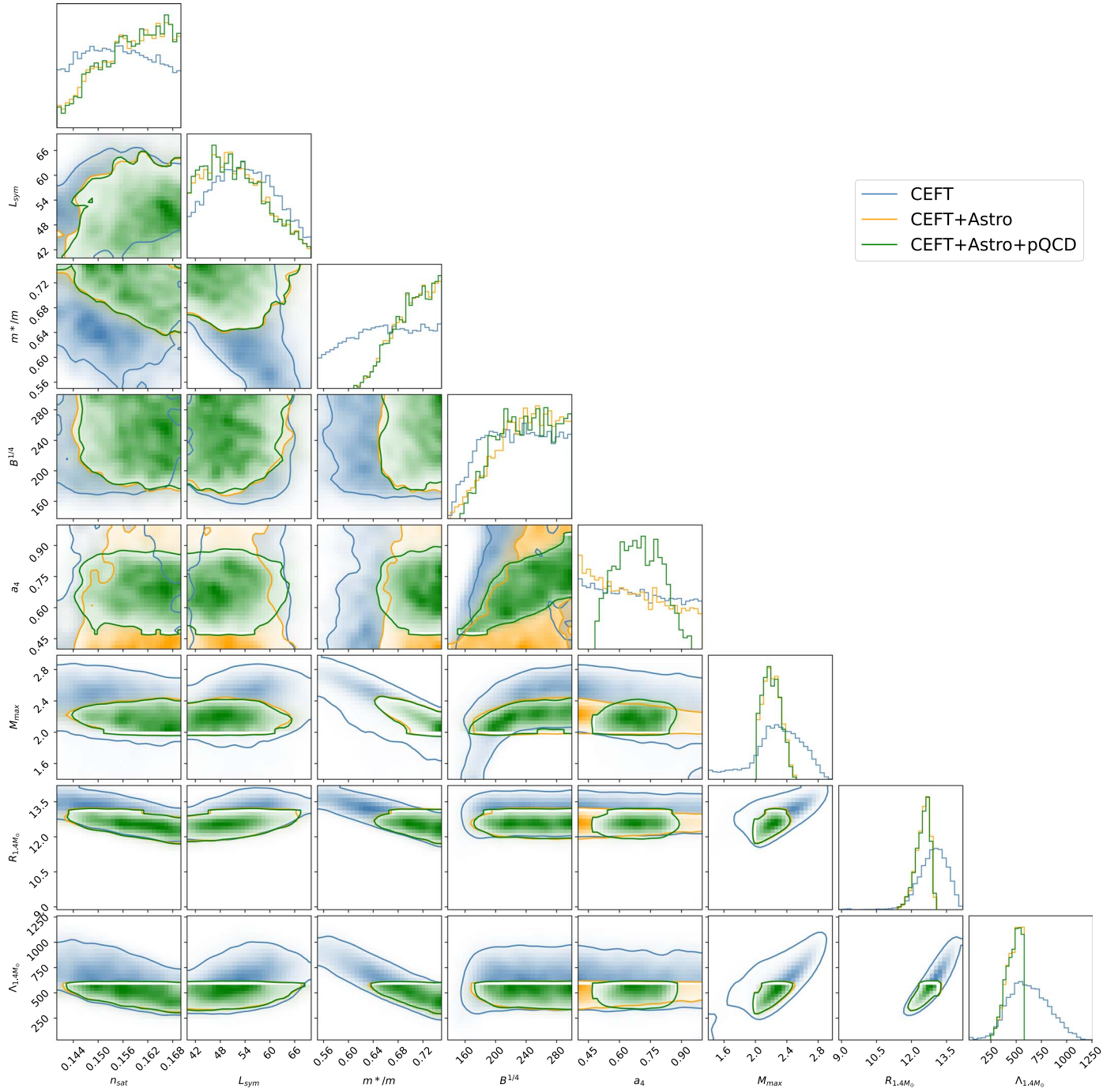

Figure 7. Posterior distributions of model parameters and NS observables that are strongly correlated presented in a corner plot after application of various filters. The color scheme is the same as in Figure 1.

solutions are obtained for low values of B. The blue points represent the EoS consistent with CEFT. The orange dots are obtained on the inclusion of astrophysical constraints. Imposing the pQCD constraint results in the green dots, further constraining the B–a_4 parameter space. We also note that this analysis puts a lower limit on the value of $a_4 \approx 0.48$. There is no strict upper limit on a_4 as it depends on the range of $B^{1/4}$ chosen. Similarly, we have a lower limit on the value of $B^{1/4} \approx 137$ MeV purely from physical considerations. The inclusion of astrophysical and pQCD constraints raises this limit to around 153 MeV.

In the scatter plot in Figure 10, we analyze the phases of matter realized for maximum-mass NSs, for the values of B–a_4 considered in Figure 9. For each EoS, we compare the critical densities for the mixed and pure quark phase with the central densities of the maximum-mass NS configuration for that EoS. For region IV, marked in yellow, the central densities are lower than the critical densities; hence, hybrid stars are not realized for such parameter values. For region III, in green, the central densities are higher than only the critical densities for the mixed phase, resulting in hybrid stars with only the mixed phase in the core. Region II, in blue, corresponds to hybrid

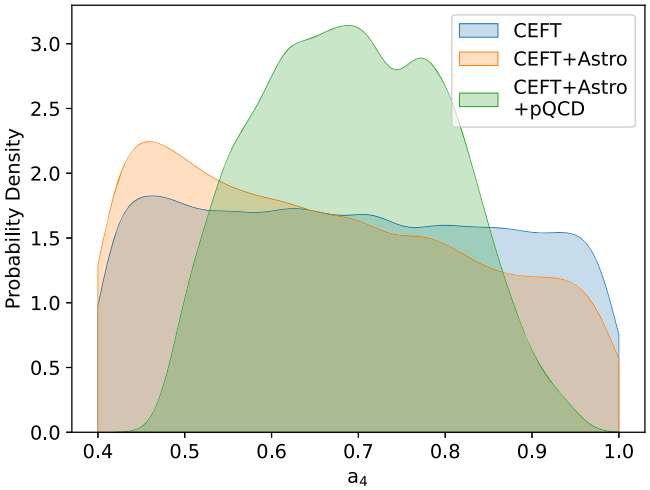

Figure 8. The change in the probability distribution of bag model parameter a_4 as a result of different constraint filters.

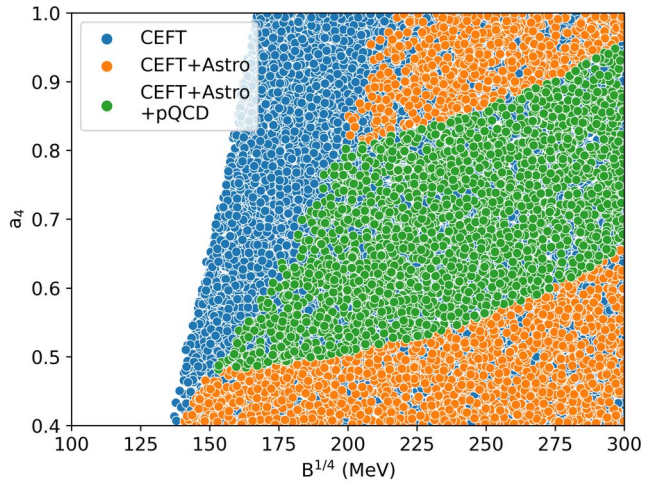

Figure 9. Scatter plot of B–a_4 parameters as a result of different filters. Same color scheme as in Figure 1 is used.

stars whose cores have a pure quark phase. Only values of $a_4 \gtrsim 0.5$ and $B^{1/4} \lesssim 185$ MeV result in a NS with a pure quark core. Region I corresponds to low values of B–a_4 for which no stable solutions for hybrid stars are obtained. A comparison of Figure 10 with Figure 9 reveals that region III (hybrid stars with mixed-phase cores) are allowed by combined filters, whereas region II (hybrid stars with a pure quark phase in the core) are disfavored by astrophysical constraints.

4. Discussions

In this work, we perform a systematic investigation of the role of EoS model parameters, both in the pure nucleonic and quark matter phases, in governing NS global observable properties. For this, we vary the model parameters (RMF model for the hadronic sector and MIT bag model for the quark sector) within their present uncertainties to generate a flat prior within a Bayesian framework with a hard cutoff. We then impose constraints from CEFT at low densities, state-of-the-art astrophysical data from electromagnetic and GW observations at high densities, and pQCD at very high densities to significantly restrict the allowed parameter space. We then use the posteriors to investigate possible

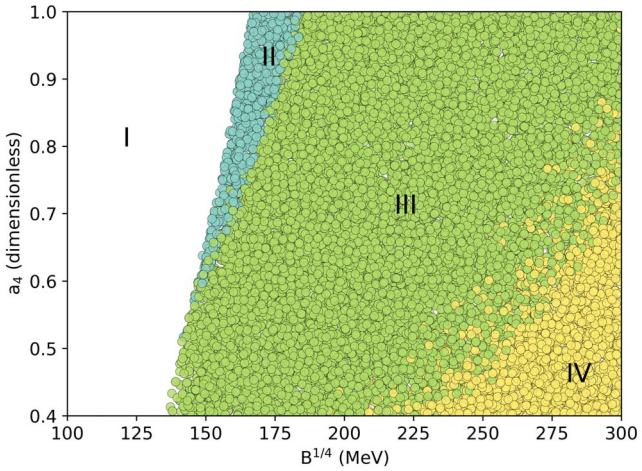

Figure 10. Different phases of matter realized in the maximum-mass NS core across the B–a_4 plane (see text for details).

correlations among the model parameters and with NS observables and extend the previous work (Ghosh et al. 2022a) to include hadron–quark phase transition.

While the CEFT calculations constrain the EoS at low densities, NS astrophysical filters imposed constraints on the allowed parameter space for the nucleonic sector at higher densities. Although pQCD calculations are effective only at very high densities, which are not attained in a NS interior, they significantly constrain the B–a_4 parameter space of the quark model and the high-density EoS. After applying the astrophysical and pQCD filters in addition to CEFT, our analysis showed that the maximum density reached inside NSs is 1.23 fm^{-3} and the maximum baryon chemical potential reached is 1.96 GeV. We do not encounter any configuration with mass greater than 2.52 $M_\odot$. We also obtain a bound on tidal deformability $\Lambda_{1.4\,M_\odot} > 247$. We get a fairly narrow range for the radius of 1.4 $M_\odot$ NS as $R_{1.4\,M_\odot} \in [11.4, 13.1]$ km. Among the bag model parameters we obtain a lower limit on $a_4 > 0.48$ and $B^{1/4} > 153$ MeV.

Next, we looked for physical correlations among model parameters and NS observables after applying different filters. First, after applying the CEFT constraints, we found a moderate correlation between $E_{\rm sym}$ and $L_{\rm sym}$. m^*/m was strongly correlated with all the NS observables except $M_{\rm max}$. $M_{\rm max}$ also showed moderate correlation with $B^{1/4}$. Addition of astrophysical filters strengthened the correlation between $E_{\rm sym}$ and $L_{\rm sym}$ and between m^*/m and $M_{\rm max}$, making m^*/m the most important parameter determining NS observables. The bag model parameters ($B^{1/4}$, a_4) did not show significant correlation with any other parameter or NS observable. However, note that there are also other observables dependent on quark content that should be studied (Alford et al. 2019). A moderate correlation between $n_{\rm sat}$ and $R_{1.4\,M_\odot}$ and a weak correlation between $L_{\rm sym}$ and $R_{1.4M_\odot}$ was seen in both cases. On applying all the filters, CEFT, astrophysical, and pQCD, we found a moderate correlation of $B^{1/4}$ with $M_{\rm max}$ and R. The most important result of the study is that we find the emergence of correlation between the bag parameters $B^{1/4}$ and a_4 due to pQCD constraints. Other correlations remain unaffected.

We performed a detailed study of the bag model parameter space upon application of the different filters. We found that astrophysical observations favor higher values of bag

constant B. Imposing the pQCD constraint along with astrophysical filters significantly restricts the B–a_4 parameter space. We also studied the phases of matter realized in the maximum NS configuration across the B–a_4 plane and found that although hybrid stars with mixed phase in the interior were allowed by some configurations, astrophysical observations disfavored the existence of pure quark matter phase in the core.

4.1. Comparison with Other Works

As outlined in Section 1, information from CEFT, multimessenger astrophysical data, or pQCD has been used previously within interpolation or Bayesian schemes to constrain the EoS in hybrid stars. However, such studies mostly employed polytropic models or constant speed-of-sound parameterizations, which do not convey information about the underlying dense hadronic or quark matter. The advantage of our scheme is that one can directly probe the effect of each of these constraints on the EoS as well as on the physical correlations among the model parameters and NS observables.

In our investigation, we employed the RMF framework for the hadronic and MIT bag model for the quark matter sector. Although few studies have been performed for hybrid stars using such models, selected RMF parameterizations were used to conclude which of them are compatible with current observations (Nandi & Char 2018; Nandi & Pal 2021; Parisi et al. 2021). In contrast, we perform a systematic investigation spanning the entire allowed parameter space (which includes such parameterizations), which allows us to investigate the role of each nuclear or quark matter parameter in governing the global NS properties through correlation studies.

The range of posteriors in $M_{\rm max}$ and $R_{1.4M_\odot}$ resulting from the different filter functions (see Table 2) can be compared to those in Table 1 of Annala et al. (2018), where only polytropes were used. Our results are consistent with those obtained by Kurkela et al. (2014), who did not realize any configuration above 2.5 $M_\odot$. Annala et al. (2018) obtained the range for mass as 2.0–2.7 $M_\odot$. The range for $R_{1.4M_\odot}$ we obtain (11.4–13.1 km) is narrower compared to previous works that use only polytropic EoS. Hebeler et al. (2013) obtained a range for $R_{1.4M_\odot}$ as 10–13.7 km applying CEFT and a maximum-mass constraint of 1.97 $M_\odot$. Kurkela et al. (2014) imposed the pQCD constraint with a mass threshold of 2 $M_\odot$ to obtain a slightly shifted range of 11–14.5 km. Annala et al. (2018) further imposed the constraint of tidal deformability of GW170817 and obtained a range of 10.7–13.6 km (one should note that the upper limit on $\Lambda_{1.4M_\odot}$ used there is 800, instead of 580 used here). In our work, we find the highest lower bound of $R_{1.4M_\odot} > 11.4$ km. Employing the bag model and three RMF EoS, Nandi & Char (2018) obtained an upper limit of $R_{1.4M_\odot} < 13.5$ km (for $\Lambda_{1.4M_\odot} < 800$), which was later updated to include 28 RMF EoS (Nandi & Pal 2021) to obtain an improved limit of $R_{1.4M_\odot} \lesssim 13.3$ km (for $\Lambda_{1.4M_\odot} < 720$). Traversi et al. (2020) performed a similar study using the RMF model in the Bayesian framework, varying five of the nuclear empirical parameters for different types of priors, and found hints of a phase transition to a chiral symmetry restored phase predicting $R_{1.4M_\odot} \sim 12$ km. Another recent study (Huth et al. 2022), similar to Ghosh et al. (2022a), performed Bayesian analysis combining information from nuclear theory, experiments, and astrophysical observations, obtaining a radius estimate of $R_{1.4M_\odot} = 11.93^{+0.39}_{-0.41}$ km. Although these studies do not consider an explicit phase transition in their model, their results are in agreement with the range for the radius we obtain. Most et al. (2018) imposed multimessenger constraints on parametrized EoS, by modeling the phase transition with a jump in energy density leading to a separate twin branch, a new family of stars. NICER observations provide simultaneous measurement of the mass and radius of NSs. Analysis of NICER data for PSR J0030+0451 yielded an equatorial radius of $R_e = 13.02^{+1.24}_{-1.06}$ km (Miller et al. 2019) for a mass of $\sim 1.44\,M_\odot$, consistent with an independent study (Riley et al. 2019) that reported $R_e = 12.71^{+1.14}_{-1.19}$ km. Analysis of GW170817 binary NS merger data also generates a mass–radius posterior obtained for a low-spin prior (Abbott et al. 2018). The final posterior set obtained passes through 1σ contours of mass–radius distributions of both of these studies. Study of another pulsar, PSR J0740+6620 (the one with maximum mass), done by Miller et al. (2021) and Riley et al. (2021), obtained radius measurements of $R_e = 13.7^{+2.6}_{-1.5}$ km and $R_e = 12.39^{+1.30}_{-0.98}$ km, respectively, for a ~ 2 $M_\odot$ NS. The posteriors satisfy 2σ contours of the joint mass–radius distribution of this pulsar. Doroshenko et al. (2022) reported an observation of an extremely light NS with $M = 0.77^{+0.20}_{-0.17}\,M_\odot$ and $R = 10.4^{+0.86}_{-0.78}$ km. This measurement falls outside our posterior band of hybrid stars. One of the possibilities, as pointed out by Doroshenko et al. (2022), is that of a strange star. The results of our investigation also rule out tidal deformability values below 247 ($\Lambda_{1.4M_\odot} > 247$). In comparison, Annala et al. (2018) obtained a much lower limit ($\Lambda_{1.4M_\odot} > 120$).

There exist several recent papers on constraining the EoS and NS properties with input from theory and astrophysical constraints. Using EoS with continuous sound speed and nonrotating stellar models consistent with nuclear theory, pQCD, and with astronomical observations, Altiparmak et al. (2022) obtained estimates at 95% credibility of NS radii for stars with 1.4 and 2.0 $M_\odot$ to be $R_{1.4} = 12.42^{+0.52}_{-0.99}$ km and $R_{2.0} = 12.12^{+1.11}_{-1.23}$ km. Using a Bayesian nonparametric inference approach for the NS EoS, and considering astrophysical data of GW170817, PSR J0030+0451, PSR J0740+6620, and incorporating the latest constraints from CEFT and pQCD at low and very high energy densities, respectively, Han et al. (2022) deduced the maximum gravitational mass of a nonrotating cold NS to be $2.18^{+0.27}_{-0.13}\,M_\odot$. Adopting an agnostic modeling of the EoS, Ecker & Rezzolla (2023) found that assuming $M_{\rm TOV} > 2.35\,M_\odot$ (Romani et al. 2022) pushes the lower bounds for NS stellar radii to significantly larger values than NICER measurements. Using a general NS EoS that parametrizes the hadron–quark phase transition between the model describing the hadronic phase and a constant speed of sound for the quark phase, Montaña et al. (2019) performed an extensive analysis of the phase transition leading to twin-star configurations and obtained limits for the maximum mass, minimum radius, and minimum tidal deformability of a $1.4\,M_\odot$ star. There also exist several older works (Köppel et al. 2019; Bauswein et al. 2017) and a rather recent work (Tootle et al. 2021) that obtained lower bounds on NS radii from threshold mass simulations in binary NS mergers.

Figure 11 shows the posterior EoS bands, as shown in Figure 1, with pressure as a function of energy density. We confirm that the CEFT constraints are most important for low

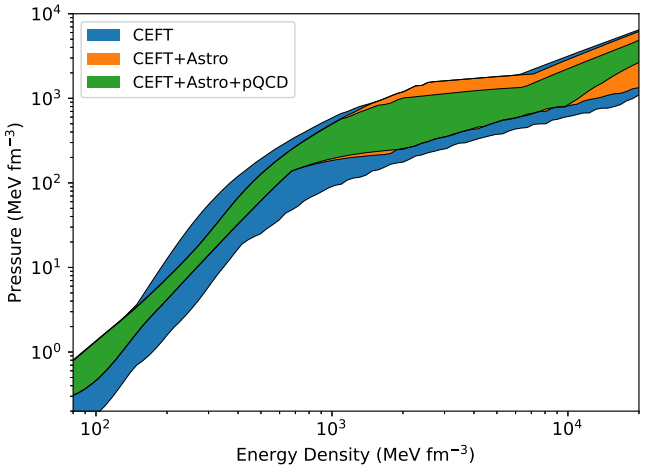

Figure 11. EoS (pressure vs. energy density) contours corresponding to the EoS contours shown in Figure 1.

energy densities. In the energy density range 100–1000 MeV fm^{-3}, the astrophysical constraints are most constraining. pQCD effects are effective at very high densities corresponding to energy density >10,000 MeV fm^{-3}. We find a kink in the EoS at around 600–700 MeV fm^{-3}, indicating the onset of the hadron–quark phase transition. This was recently proposed as strong evidence for the existence of quark matter (see Figure 10 of Kurkela et al. 2014, Figure 3 of Annala et al. 2018, and Figure 1 of Annala et al. 2020).

For a fixed RMF EoS (NL3$\omega\rho$), Nandi & Char (2018) reported upper limits of 163 MeV for $B^{1/4}$ and 0.65 for a_4. Varying all the model parameters within their present uncertainties and imposing multiphysics and multimessenger constraints, we obtain a lower limit of $a_4 > 0.48$. From our analysis of Figure 10, for most of the bag parameter values, NSs with a mixed core are realized (region III), while a pure quark core is formed for a narrow band represented by region II. This is in contrast with the findings of Nandi & Pal (2021), which reported a mixed-phase core for most of the hybrid stars but also several EoS with pure quark cores. Our results are, however, consistent with the findings of Weissenborn et al. (2011), which studied hybrid stars considering two RMF EoS (TM1 and NL3) and found pure quark cores for a very small parameter range. They concluded that a pure quark core appears if the phase transition begins around nuclear saturation density, which happens in the case of low $B^{1/4}$ and high a_4.

Using the speed-of-sound parameterization, Annala et al. (2020) used the criterion on the polytropic index $\gamma < 1.75$ (an average between CET and pQCD values) to determine the presence of a quark core. They concluded that if $c_s^2 < 0.4$ the quark core may be substantial but if $c_s^2 > 0.5$, i.e., if stars have maximum mass $>2.25\,M_\odot$, the quark core may be small or absent in $2\,M_\odot$ stars. The same criterion of $\gamma < 1.75$ was applied in Han et al. (2022) to determine the presence of quark matter within a nonparametric scheme. In our work, instead of using a criterion based on the polytropic index, we determine the hadron–quark phase transition using a microscopic model, where Gibbs phase rules are applied to describe the mixed phase. With the advantage of our model framework, we could arrive at the conclusion that on demanding compatibility with astrophysical constraints, a pure quark core is disfavored but mixed-phase cores are favored. However, this also confirms observation of a softening of the EoS and a phase transition is expected. Therefore our results are not in contradiction with results from Annala et al. (2020) and Han et al. (2022), as they use the polytropic index only to denote the onset of quark matter, which need not necessarily be a pure quark matter phase. It is also consistent with Ecker & Rezzolla (2022), who observe softening of the EoS in NS cores.

4.2. Implications and Future Directions

This work is the first systematic study of the application of combined filters from nuclear physics calculations, astrophysical data, and pQCD to restrict the range of model parameters in hybrid stars for realistic EoS. The results of this study clearly identify the effect of each of the filters on the underlying empirical parameters and correlations, as well as the role of the parameters in governing NS observables. This could help significantly reduce the parameter space and, therefore, the computational time for parameter estimation for future GW searches. The analysis also imposes strong restrictions on the allowed parameter space of the widely used bag model using the combined filters and also draws important conclusions about the possibility of finding quark matter in the interior of hybrid stars.

From this work on NS astrophysical observables, it would be interesting to investigate the consequences of the restricted parameter space (particularly for the bag model). Our allowed parameter space disfavors hybrid stars with a pure quark phase but allows a mixed phase in the interior. We leave this for a possible future investigation.

The authors acknowledge usage of the IUCAA HPC computing facility for numerical calculations. S.S. would like to thank Bikram Keshari Pradhan and Dhruv Pathak for useful discussions during this work. The authors also thank the anonymous referee whose thoughtful suggestions helped to improve our manuscript.

Appendix
Speed of Sound

All the hybrid EoS generated transition to quark EoS at high densities via a mixed phase. The speed of sound contours for these are plotted in Figure 12. The behavior of the speed of sound curves in each of the three phases (hadronic, mixed, and pure quark) is similar to that obtained in Figure 2 of Han et al. (2019) for hybrid EoS using a Gibbs construction with the high-density speed of sound controlled by the interaction parameter "a" of the quark model. The speed of sound discontinuously increases to that of the quark phase at the end of the mixed phase. The maximum speed of sound observed in the final quark phase is 0.332, in units of speed of light. Thus, the speed of sound is observed to approach the conformal limit ($c_s^2 = 1/3$) from below at high densities. We further note that the maximum speed of sound reached for EoS that satisfy all the constraints is $c_s^2 \sim 0.8$. EoS consistent with the astrophysical observations reach at least $c_s^2 \sim 0.35$ at some intermediate density. So, we conclude for the current formalism that violation of the conformal limit is required to explain massive NSs. This is in accordance with the recent findings of Altiparmak et al. (2022), where only 0.03% of the EoS satisfying all the constraints were found to be sub-conformal.

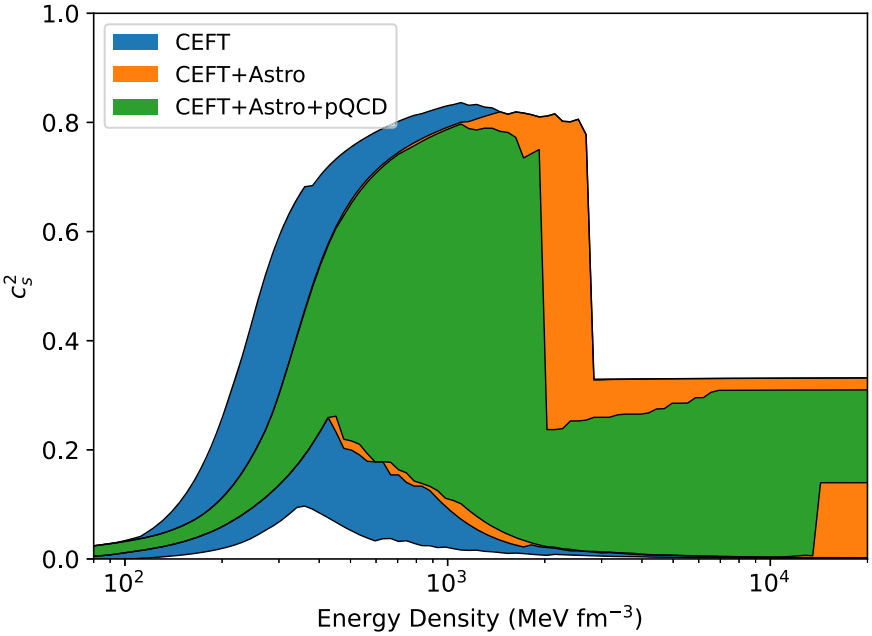

Figure 12. Contours of speed of sound (in units of speed of light) as a function of energy density corresponding to the EoS contours shown in Figure 1.

ORCID iDs

Swarnim Shirke https://orcid.org/0000-0001-8604-5362
Suprovo Ghosh https://orcid.org/0000-0002-1656-9870
Debarati Chatterjee https://orcid.org/0000-0002-0995-2329

References

Abbott, B. P., Abbott, R., Abbott, T. D., et al. 2017a, PhRvL, 119, 161101
Abbott, B. P., Abbott, R., Abbott, T. D., et al. 2017b, ApJL, 848, L13
Abbott, B. P., Abbott, R., Abbott, T. D., et al. 2018, PhRvL, 121, 161101
Abbott, B. P., Abbott, R., Abbott, T. D., et al. 2019, PhRvX, 9, 011001
Adhikari, D., Albataineh, H., Androic, D., et al. 2021, PhRvL, 126, 172502
Alam, N., Agrawal, B. K., Fortin, M., et al. 2016, PhRvC, 94, 052801
Alford, M., Blaschke, D., Drago, A., et al. 2007, Natur, 445, 7
Alford, M. G., Han, S., & Prakash, M. 2013, PhRvD, 88, 083013
Alford, M. G., Han, S., & Schwenzer, K. 2019, JPhG, 46, 114001
Altiparmak, S., Ecker, C., & Rezzolla, L. 2022, ApJL, 939, L34
Annala, E., Gorda, T., Katerini, E., et al. 2022, PhRvX, 12, 011058
Annala, E., Gorda, T., Kurkela, A., Nättilä, J., & Vuorinen, A. 2020, NatPh, 16, 907
Annala, E., Gorda, T., Kurkela, A., & Vuorinen, A. 2018, PhRvL, 120, 172703
Antoniadis, J., Freire, P. C. C., Wex, N., et al. 2013, Sci, 340, 448
Aoki, Y., Endrődi, G., Fodor, Z., Katz, S. D., & Szabó, K. K. 2006, Natur, 443, 675
Bauswein, A., Bastian, N. U. F., Blaschke, D. B., et al. 2019, PhRvL, 122, 061102
Bauswein, A., Just, O., Janka, H.-T., & Stergioulas, N. 2017, ApJL, 850, L34
Baym, G., Hatsuda, T., Kojo, T., et al. 2018, RPPh, 81, 056902
Bazavov, A., Ding, H. T., Hegde, P., et al. 2017, PhRvD, 95, 054504
Bazavov, A., Ding, H. T., Hegde, P., et al. 2019, PhLB, 795, 15
Biswas, B. 2021, ApJ, 921, 63
Bogdanov, S., Heinke, C. O., Özel, F., & Güver, T. 2016, ApJ, 831, 184
Chatterjee, D., Gulminelli, F., Raduta, A., & Margueron, J. 2017, PhRvC, 96, 065805
Chatziioannou, K., & Han, S. 2020, PhRvD, 101, 044019
Chen, W. C., & Piekarewicz, J. 2014, PhRvC, 90, 044305
Chodos, A., Jaffe, R. L., Johnson, K., & Thorn, C. B. 1974a, PhRvD, 10, 2599
Chodos, A., Jaffe, R. L., Johnson, K., Thorn, C. B., & Weisskopf, V. F. 1974b, PhRvD, 9, 3471
Coughlin, M. W., Dietrich, T., Margalit, B., & Metzger, B. D. 2019, MNRAS, 489, L91
Cromartie, H. T., Fonseca, E., Ransom, S. M., et al. 2020, NatAs, 4, 72
Damour, T., & Nagar, A. 2009, PhRvD, 80, 084035
de Forcrand, P. 2010, arXiv:1005.0539
Demorest, P. B., Pennucci, T., Ransom, S. M., Roberts, M. S. E., & Hessels, J. W. T. 2010, Natur, 467, 1081
Dietrich, T., Coughlin, M. W., Pang, P. T. H., et al. 2020, Sci, 370, 1450
Doroshenko, V., Suleimanov, V., Pühlhofer, G., & Santangelo, A. 2022, NatAs, 6, 1444
Drischler, C., Carbone, A., Hebeler, K., & Schwenk, A. 2016, PhRvC, 94, 054307
Drischler, C., Hebeler, K., & Schwenk, A. 2019, PhRvL, 122, 042501
Ecker, C., & Rezzolla, L. 2022, ApJL, 939, L35
Ecker, C., & Rezzolla, L. 2023, MNRAS, 519, 2615
Farhi, E., & Jaffe, R. L. 1984, PhRvD, 30, 2379
Fattoyev, F. J., Carvajal, J., Newton, W. G., & Li, B.-A. 2013, PhRvC, 87, 015806
Fattoyev, F. J., & Piekarewicz, J. 2010, PhRvC, 82, 025805
Fattoyev, F. J., Piekarewicz, J., & Horowitz, C. J. 2018, PhRvL, 120, 172702
Flanagan, É. É., & Hinderer, T. 2008, PhRvD, 77, 021502
Fodor, Z., & Katz, S. D. 2004, JHEP, 2004, 050
Fonseca, E., Cromartie, H. T., Pennucci, T. T., et al. 2021, ApJL, 915, L12
Fraga, E. S., Kurkela, A., & Vuorinen, A. 2014, ApJL, 781, L25
Ghosh, S., Chatterjee, D., & Schaffner-Bielich, J. 2022a, EPJA, 58, 37
Ghosh, S., Pradhan, B. K., Chatterjee, D., & Schaffner-Bielich, J. 2022b, FrASS, 9, 864294
Glendenning, N., & Moszkowski, S. 1991, PhRvL, 67, 2414
Glendenning, N. K. 1997, Compact Stars: Nuclear Physics, Particle Physics and General Relativity (New York: Springer)
Gorda, T., Kurkela, A., Paatelainen, R., Säppi, S., & Vuorinen, A. 2021a, PhRvD, 104, 074015
Gorda, T., Kurkela, A., Paatelainen, R., Säppi, S., & Vuorinen, A. 2021b, PhRvL, 127, 162003
Gorda, T., Kurkela, A., Romatschke, P., Säppi, M., & Vuorinen, A. 2018, PhRvL, 121, 202701
Guillot, S., Servillat, M., Webb, N. A., & Rutledge, R. E. 2013, ApJ, 772, 7
Han, M. Z., Huang, Y. J., Tang, S. P., & Fan, Y. Z. 2022, arXiv:2207.13613
Han, S., Mamun, M. A. A., Lalit, S., Constantinou, C., & Prakash, M. 2019, PhRvD, 100, 103022
Hebeler, K., Lattimer, J. M., Pethick, C. J., & Schwenk, A. 2013, ApJ, 773, 11
Hinderer, T. 2008, ApJ, 677, 1216
Hornick, N., Tolos, L., Zacchi, A., Christian, J.-E., & Schaffner-Bielich, J. 2018, PhRvC, 98, 065804
Huth, S., Pang, P. T. H., Tews, I., et al. 2022, Natur, 606, 276
Keller, J., Wellenhofer, C., Hebeler, K., & Schwenk, A. 2021, PhRvC, 103, 055806
Keshari Pradhan, B., Chatterjee, D., Gandhi, R., & Schaffner-Bielich, J. 2023, NuPhA, 1030, 122578
Komoltsev, O., & Kurkela, A. 2022, PhRvL, 128, 202701

Köppel, S., Bovard, L., & Rezzolla, L. 2019, ApJL, 872, L16
Kovács, P., Takátsy, J., Schaffner-Bielich, J., & Wolf, G. 2022, PhRvD, 105, 103014
Kurkela, A., Fraga, E. S., Schaffner-Bielich, J., & Vuorinen, A. 2014, ApJ, 789, 127
Kurkela, A., Romatschke, P., & Vuorinen, A. 2010, PhRvD, 81, 105021
Lattimer, J. M., & Lim, Y. 2013, ApJ, 771, 51
Lattimer, J. M., & Prakash, M. 2004, Sci, 304, 536
Li, A., Zhu, Z. Y., Zhou, E. P., et al. 2020, JHEAp, 28, 19
Lim, Y., & Holt, J. W. 2018, PhRvL, 121, 062701
Linares, M. 2020, in Multifrequency Behaviour of High Energy Cosmic Sources (MULTIF2019), 23
Linares, M., Shahbaz, T., & Casares, J. 2018, ApJ, 859, 54
Margalit, B., & Metzger, B. D. 2017, ApJL, 850, L19
Margueron, J., Hoffmann Casali, R., & Gulminelli, F. 2018, PhRvC, 97, 025806
Miller, M. C., Lamb, F. K., Dittmann, A. J., et al. 2019, ApJL, 887, L24
Miller, M. C., Lamb, F. K., Dittmann, A. J., et al. 2021, ApJL, 918, L28
Montaña, G., Tolós, L., Hanauske, M., & Rezzolla, L. 2019, PhRvD, 99, 103009
Most, E. R., Weih, L. R., Rezzolla, L., & Schaffner-Bielich, J. 2018, PhRvL, 120, 261103
Müller, H., & Serot, B. D. 1996, NuPhA, 606, 508
Nambu, Y., & Jona-Lasinio, G. 1961a, PhRv, 122, 345
Nambu, Y., & Jona-Lasinio, G. 1961b, PhRv, 124, 246
Nandi, R., & Char, P. 2018, ApJ, 857, 12
Nandi, R., & Pal, S. 2021, EPJST, 230, 551
Nättilä, J., Miller, M. C., Steiner, A. W., et al. 2017, A&A, 608, A31
Oertel, M., Hempel, M., Klähn, T., & Typel, S. 2017, RvMP, 89, 015007
Özel, F., & Freire, P. 2016, ARA&A, 54, 401
Özel, F., Psaltis, D., Arzoumanian, Z., Morsink, S., & Bauböck, M. 2016, ApJ, 832, 92
Pang, P. T. H., Dietrich, T., Tews, I., & Van Den Broeck, C. 2020, PhRvR, 2, 033514
Pang, P. T. H., Tews, I., Coughlin, M. W., et al. 2021, ApJL, 922, 14
Parisi, A., Vasquez Flores, C., Lenzi, C. H., Chen, C.-S., & Lugones, G. 2021, JCAP, 2021, 042
Paschalidis, V., Yagi, K., Alvarez-Castillo, D., Blaschke, D. B., & Sedrakian, A. 2018, PhRvD, 97, 084038
Raaijmakers, G., Greif, S. K., Riley, T. E., et al. 2020, ApJL, 893, L21
Radice, D., & Dai, L. 2019, EPJA, 55, 50
Radice, D., Perego, A., Zappa, F., & Bernuzzi, S. 2018, ApJL, 852, L29
Reed, B. T., Fattoyev, F. J., Horowitz, C. J., & Piekarewicz, J. 2021, PhRvL, 126, 172503
Rezzolla, L., Most, E. R., & Weih, L. R. 2018, ApJL, 852, L25
Riley, T. E., Watts, A. L., Bogdanov, S., et al. 2019, ApJL, 887, L21
Riley, T. E., Watts, A. L., Ray, P. S., et al. 2021, ApJL, 918, L27
Romani, R. W., Kandel, D., Filippenko, A. V., Brink, T. G., & Zheng, W. 2022, ApJL, 934, L17
Schaffner-Bielich, J. 2020, Compact Star Physics (Cambridge: Cambridge Univ. Press), doi:10.1017/9781316848357
Tolos, L., Centelles, M., & Ramos, A. 2017, ApJ, 834, 3
Tootle, S. D., Papenfort, L. J., Most, E. R., & Rezzolla, L. 2021, ApJL, 922, L19
Traversi, S., Char, P., & Pagliara, G. 2020, ApJ, 897, 165
Weber, F. 1999, Pulsars as Astrophysical Laboratories for Nuclear and Particle Physics (London: Taylor and Francis)
Weissenborn, S., Sagert, I., Pagliara, G., Hempel, M., & Schaffner-Bielich, J. 2011, ApJL, 740, L14
Xie, W.-J., & Li, B.-A. 2021, PhRvC, 103, 035802
Yagi, K., & Yunes, N. 2013, PhRvD, 88, 023009
Zhang, N.-B., & Li, B.-A. 2019, JPhG, 46, 014002
Zhou, E.-P., Zhou, X., & Li, A. 2018, PhRvD, 97, 083015
Zhu, Z.-Y., Zhou, E.-P., & Li, A. 2018, ApJ, 862, 98